Journal of Manufacturing Processes 62 (2021) 302–312

Contents lists available at ScienceDirect

Journal of Manufacturing Processes

journal homepage: www.elsevier.com/locate/manpro

3D finite element model of dynamic material behaviors for multilayer ultrasonic metal welding

Ninggang Shen [a], Avik Samanta [a], Wayne W. Cai [b], Teresa Rinker [b], Blair Carlson [b], Hongtao Ding [a,*]

[a] Department of Mechanical Engineering, University of Iowa, Iowa City, IA, 52242, USA
[b] Manufacturing Systems Research Lab, General Motors R&D Center, Warren, MI, 48090, USA

ARTICLE INFO

Keywords:
Ultrasonic metal welding
Modeling
Finite element method
Dynamic welding force

ABSTRACT

Ultrasonic metal welding (UMW) has been widely applied as a high throughput solid-state joining technology for multilayers of sheet metal. During a typical UMW process, multilayer work materials are mechanically compressed by a knurl-patterned horn (also known as a sonotrode) onto an anvil tool, and a simultaneous in-plane sliding is applied to the horn at an ultrasonic frequency (20 kHz or higher) to help form the weld at the material interfaces. There is a great challenge in modeling and simulating the dynamic behavior of the work material and the whole weld formation process is subject to ultrasonic mechanical loadings imposed by the knurl-patterned horn tool. In this work, finite element (FE) models are developed to simulate the multilayer UMW process using knurl-patterned tools by directly applying the ultrasonic vibration as a model input. For a short weld duration of 0.1~0.5 s, a high-fidelity FE modeling approach is developed using ABAQUS/Explicit to simulate the dynamic material response under the 20 kHz horn vibration. For an extended long welding duration of approximately 1.0 s, a computationally efficient hybrid approach is developed using both ABAQUS/Explicit and DEFORM-3D in order to leverage the strengths of each software package. The developed models are validated using experimental data of dynamic welding force, temperature, and weld geometry from in-situ process measurements of UMW. The 3D FE models developed in this study are the most comprehensive solution to date to simulate the complex material response subject to UMW process conditions and provide engineering guidance for the design of UMW applications.

1. Introduction

Ultrasonic metal welding (UMW) has been widely applied as a solid-state joining technology for multilayer malleable materials [1]. UMW is a high throughput process for joining both similar and dissimilar materials due to its fast processing speed (e.g., UMW process duration for welding a single weld is typically 0.5~1 s), low energy consumption, low cost, and environment-friendliness [2,3]. Taking advantage of UMW's solid-state joining nature for dissimilar materials, it has been extensively applied to join aluminum and copper tabs in lithium-ion battery cells for electric vehicles [2] and other applications for electronic components [4–8]. During a typical UMW process, sheet metal materials are mechanically compressed by knurl-patterned welder horn (also known as a sonotrode) onto anvil tool, and simultaneously in-plane sliding is applied to the horn at an ultrasonic frequency (20 kHz or higher) to help form the weld between the work materials. Ultrasonic vibration energy is mostly consumed at the work material interfaces, resulting in a significant temperature increase, severe plastic deformation, and solid-state bonding.

The processing principles of UMW have been extensively investigated using experimental approaches in past decades. The mechanical system response of the UMW machine configuration was studied using analytical models to determine the effect of ultrasonic loading on the weld quality [9,10]. Various UMW process parameters such as welding energy and welding process duration have been investigated to evaluate the welding quality defined by weld nugget size, bond density, post-weld thickness, and thermomechanically affected zone size [2,11]. Zhao et al. developed a fatigue life cycle model based on the monitoring of electrical resistance to foresee the life of ultrasonic weld aluminum (Al)/copper (Cu) tab joints [12]. The weld strength by UMW and its microstructural attributes particularly at the welding interface were found to be dependent on these processing parameters [2]. Formation of

* Corresponding author.
E-mail address: hongtao-ding@uiowa.edu (H. Ding).

https://doi.org/10.1016/j.jmapro.2020.12.039
Received 19 August 2020; Received in revised form 7 December 2020; Accepted 12 December 2020

intermetallic compound (IMC) has been reported at the weld interface during the UMW process of dissimilar materials [7,13,14]. Process robustness and layer-wise microstructures were studied for multilayer UMW process with dissimilar material combinations [15,16]. Particularly, diffusion bonding has been observed at the interface between copper and aluminum for an extended period of welding time [7,14,17–20]. The diffusion phenomena at the joining interface were also investigated through molecular dynamics simulation [5,21]. Online monitoring systems have been developed to monitor and measure the dynamic welding power and horn displacement during the process [11,22]. Lee et al. [23] analyzed displacement of tool and coupons during the multilayer UMW process using a high-speed imaging technique and demonstrated that weld quality deteriorated from top to bottom layers due to less heat generation at the interfaces of bottom layers. In-situ monitoring and measurement of UMW process provide critical processing information, including horn movement, temperature history, force history, and power requirement [11,24–26]. Additionally, monitoring the tool wear at different stages of tool-life is important to have good weld quality [27,28].

Process modeling and simulation are important for designing and optimizing the UMW process by linking its process parameters and weld properties and performance. For instance, process models can provide insights on the design of knurl geometry by providing its effect on the contact and friction behavior of the joint formation [29,30]. They can also help provide understandings on the heat generation and deformation at the joint interface that greatly influence the weld quality [31,32]. However, great challenges exist to date preventing the development of computationally efficient UMW process models. First challenge is to model the strong coupling effects among the mechanical, thermal, and metallurgical fields. During the UMW process, materials undergo nonlinear hardening under 20 kHz cyclic loading and predominately friction-induced thermal softening, which affects heat generation [30,33]. Additionally, materials often exhibit a significant acoustic softening under ultrasonic loading [34,35], which reduces the flow stress during the operation. The acoustic energy of the ultrasonic sonotrode transfers into the working material and is consumed at defects of the crystalline lattice, including dislocations, vacancies, and grain boundaries [34]. Consequently, the activation energy required for the movement of dislocations is substantially lowered [35]. Experimental investigation and dislocation dynamics simulation have shown that application of ultrasonic vibration during material deformation can result in reduction of dislocation density and/or subgrain formation [36–39]. Therefore, the acoustic softening effect is an intrinsic material phenomenon that prompts dislocation annihilation and/or subgrain formation [38]. To consider the acoustic softening effect, Siddiq and Ghassemieh [40] introduced an empirical term on flow stress calculation using a phenomenological constitutive model to combine with the kinematic hardening model under cyclic loading. They incorporated the constitutive flow stress model in a three-dimensional (3D) thermomechanical FE model for an ultrasonic seam welding process and predicted weld material response under applied load, ultrasonic vibration amplitude, and tool velocity [40,41].

The second challenge is to model the dynamic weld formation process and capture the detailed material response under constraints imposed by the 3D geometry of UMW welder tools and high frequency vibration loading. Elangovan et al. [33] developed a FE model to simulate heat generation due to friction and deformation during UMW, while a simplified two-dimensional (2D) process setup was considered without modeling the knurl patterned tools or high frequency ultrasonic transverse movement of the tool. Lee et al. [42] developed a 3D thermomechanical FE model for multi-sheet dissimilar materials (Al and Cu) to predict temperature and stress at the welded area; however, simplified welder tool geometry was assumed without considering the knurl pattern, and the ultrasonic motion was not used as a loading condition for the tool. Shen et al. [43] developed a metallo-thermo-mechanically coupled 3D FE model to simulate both weld formation and microstructural evolution for a knurl patterned tool. 20 kHz ultrasonic loading was considered indirectly through the material modeling during the welding duration. Li et al. [44] developed a 3D thermomechanical FE model for dissimilar materials (Al & Cu) in a two-layer lap welding configuration. They considered material softening, and high convection boundary conditions in their modeling approach, while ultrasonic vibration of the horn was not directly modeled. Chen et al. [45] developed a 3D thermomechanical FE model for UMW of Al-Cu stackups by directly incorporating ultrasonic vibration loading to a knurl patterned horn. The simulated welding process duration was limited to 0.05 s for a vibration amplitude of 9 μm, which is a moderate condition compared with the typical UMW conditions. Later, an enhanced FE model was developed to simulate multilayer USW of Cu with a pyramid-knurl horn tool [26]. The simulation time was extended to 0.2 s with a greater horn vibration amplitude of 23 μm, which is still a shorter duration than that of the typical UMW process.

Realizing that the duration of most ultrasonic metal welding is on the order of 0.5 s or greater, it remains a great challenge in modeling and simulating the dynamic behaviors of the work material and the full UMW process imposed by the welder tools. The process models developed in literature do not have the capability for simulating the full UMW cycle using practical 3D knurl-patterned tools. In this work, 3D numerical models were developed for the first time to simulate the complete multilayer UMW process involving complex material thermomechanical response. For a short weld duration up to 0.5 s, a high-fidelity FE modeling approach was developed using ABAQUS/Explicit to simulate the dynamic material response under the 20 kHz horn vibration. However, excessive element distortion remained a technical barrier for the high-fidelity approach as the work material was more severely deformed for longer welding durations. Therefore, for a long welding duration of approximately 1.0 s or longer, a computationally efficient hybrid approach was developed using both ABAQUS/Explicit and DEFORM-3D, which took advantage of the strengths of both software packages. The developed model will be able to provide guidance to optimized process parameters to have a good weld quality. Additionally, it will be able to provide guidance to design future knurl patterns for horn and anvil. Therefore, the developed model has significant importance for the process development in manufacturing industries.

2. In-situ monitoring and measurement of ultrasonic metal welding process

An in-situ monitoring system was implemented in this work to provide valuable dynamic attributes during the UMW process, including high-frequency dynamic welding force, temperature histories in the work materials, high-frequency vibrations of welder horn and anvil, and slippage between coupon and anvil. Four-layer UMW experiments were performed using the Stapla ultrasonic metal welder-based system. Ni-plated C11000 Cu was used as the testing material for three identical battery tabs and one busbar coupon to mimic a typical electrical battery cell joining application. Each experiment was repeated two additional times. All the testing coupons were 45 mm × 41 mm in size, while the thickness of the tab and busbar coupons was 0.2 mm and 0.9 mm, respectively. The UMW experimental parameters are listed in Table 1.

The in-situ experimental apparatus for UMW is presented in Fig. 1a

Table 1
Experimental conditions.

Tab materials	0.2 mm Ni-plated C11000 Cu (Ni coating of 0.1~0.2 μm)
Busbar material	0.9 mm Ni-plated C11000 Cu (Ni coating 1.0~2.5 μm)
Clamping pressure (bar)	4.2
Vibration amplitude (μm)	8, 30
Vibration frequency (kHz)	20
Welding energy (J)	1600, 2400, 3200

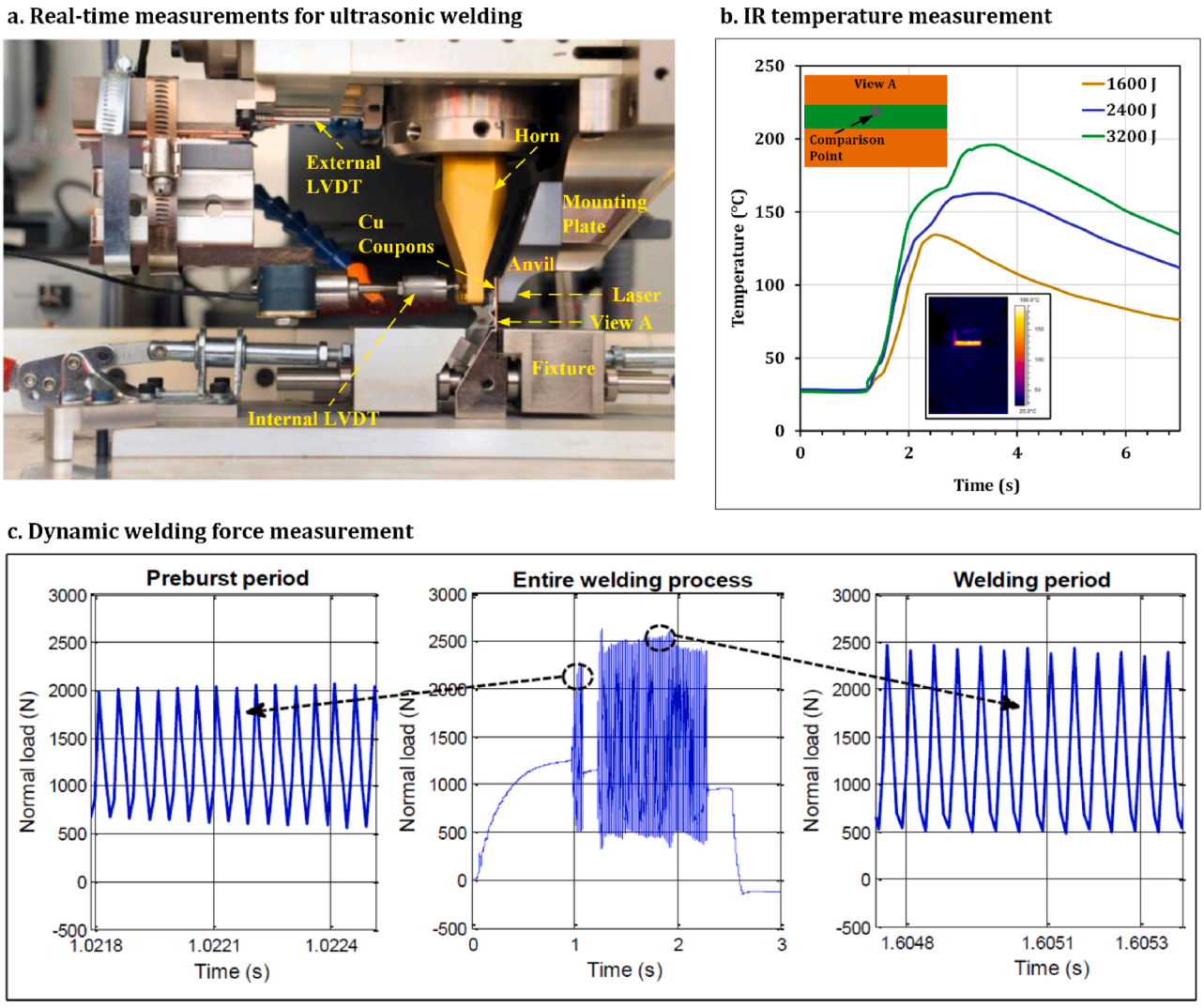

Fig. 1. Dynamic measurements for the UMW process: (a) experimental setup; (b) infrared temperature measurement; (c) dynamic welding force measurement.

with various instruments and sensors for force, temperature and vibration dynamics. The high frequency vibrations of the horn during the welding process were measured using the Polytec® (OFV 5000) single point laser vibrometer. In addition, the displacement of the horn under ultrasonic loading was measured using the Omega® LVDT sensor mounted on the welder. An infrared camera (Flir® ThermaCAM S60) was used to capture the surface temperature history of test coupons during the welding process. As a major portion of the coupons and tabs was blocked by the weld tool, temperature was only measured at the middle portion of the coupons. Emissivity tapes were used to enhance measurement sensitivity and accuracy. Reflective tapes were used to ensure good reflection of the laser beam. The infrared camera captured the temperature history on the emissivity tape covered area only as observed from View A in Fig. 1a. The temperature of only the focused area (Fig. 1b) could be captured, while other areas were blocked by the anvil and the fixture. A representative infrared image at peak temperatures for the Cu busbar coupon is presented in Fig. 1b. The temperature profiles of the Cu busbar are compared for three different ultrasonic welding energies in Fig. 1b. As the welding energy increased from 1600 J to 3200 J, the peak temperature increased from 135 °C to 195 °C. Additionally, the peak temperature position shifted towards the right, indicating that the peak temperature was achieved faster for a low welding energy as compared to a with high welding energy.

Kistler ® SlimLine 1-component load cell was embedded in the anvil mounting plate to measure the clamping and welding forces between the anvil and mounting plate. Fig. 1c are plots of representative force measurements in the normal direction versus time during UMW process at a welding energy of 2400 J and 8 μm amplitude. The force signal also follows sinusoidal fluctuation with mean value of 1500 N at a frequency of 20 kHz. The dynamic force during welding can be significantly higher than the static clamping force, varying between 500 N (valley) and 2500 N (peak).

3. Finite element models

Two 3D FE models were developed to simulate UMW of multilayer work materials. As shown in Fig. 2a, for a short welding duration of 0.1−0.5 s, the high-fidelity FE model directly modeled the ultrasonic loading as model input and simulated the whole weld formation process from knurl patterned ultrasonic tools. ABAQUS/Explicit solver with the use of Arbitrary Lagrangian-Eulerian (ALE) was selected for the high-fidelity model of the highly dynamic thermomechanically coupled UMW process imposed by 20 kHz horn vibration. Implicit time integration method available from either ABAQUS or DEFORM-3D was found not suitable for such a computation-costly simulation. The high-fidelity method was limited to a short welding duration as the simulation would abort when the weld duration was long with more severe mesh distortion. For a long welding duration such as 1.0 s with more severe plastic deformation, a computationally efficient hybrid model was developed using both ABAQUS/Explicit and DEFORM-3D as

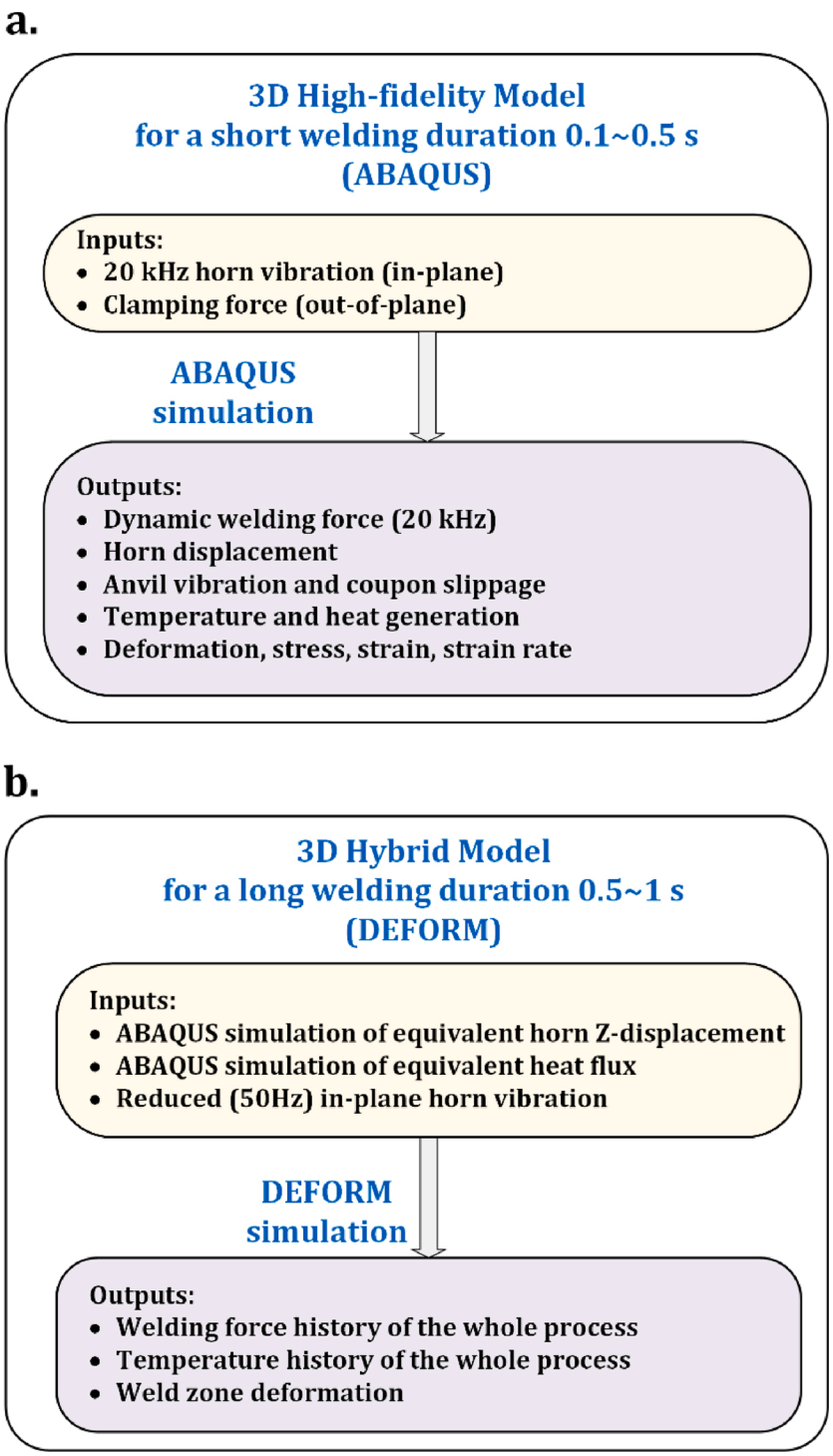

Fig. 2. 3D finite element models for ultrasonic welding.

illustrated in Fig. 2b. For the hybrid method, the DEFORM model ensured the simulation of the whole process duration while maintaining the simulation accuracy by using the high-fidelity ABAQUS model results as its inputs.

3.1. *High-fidelity model for short-duration welding*

The high-fidelity FE modeling approach used the explicit scheme in ABAQUS to simulate dynamic material response during the UMW process by directly applying the 20 kHz horn vibration as model input. For the UMW experiments described in Section 2, the Stapla ultrasonic welder horn tool comprised three identical and equally spaced welding pads. In order to reduce the computational cost, a single horn tool pad or 1/3 of the horn tool geometry was modeled in this work, and hence 1/3 of the clamping force was applied in the simulation accordingly. The horn pad with truncated pyramid knurl pattern and anvil pad with fine diamond knurl pattern were modeled respectively in this FE model, as shown in Fig. 3. For the finite element model configuration, the anvil was assumed fully rigid with constraints for all degrees of freedom. Three Cu tab layers and one Cu busbar layer were modeled as work materials. ALE adaptive meshing technique was applied to the work material domains to maintain a high-quality mesh when large

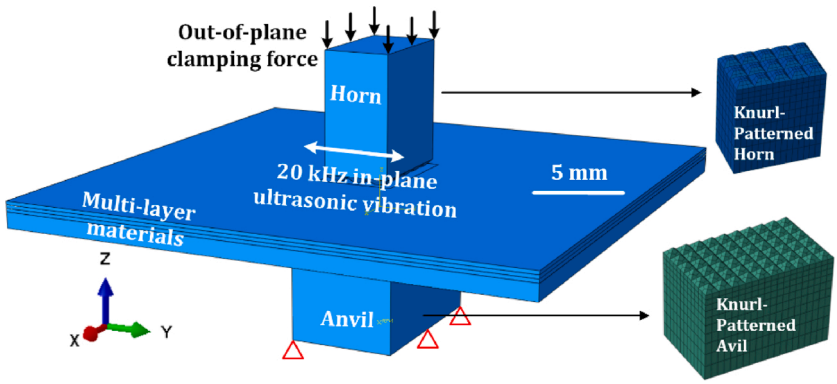

Fig. 3. 3D ABAQUS model configuration for ultrasonic welding [the scalebar represents dimension in Y direction].

deformations occurred in the weld zone.

The loadings of the welding process were defined by the vertical out-of-plane clamping force (in z-direction) and a 20 kHz in-plane vibration (x–y plane) through the simulation. The ultrasonic horn vibration was directly modeled as the loading for the horn. A 20 kHz sinusoidal vibration was applied to the horn along the y-axis in the model, refer to Fig. 3. The clamping force was modeled by a constant pressure on the horn top surface. The magnitude of this pressure was determined with the actual clamping force on this pad and the horn top surface area. Cai et al. [46] experimentally determined the friction coefficient between battery tabs and busbar during multilayer UMW process. They studied the effects of vibration frequency, condition of the surface and normal load on the friction coefficient between layers. In this model, a friction coefficient of 1.2 was adopted at the interface between tab and busbar.

3.2. Hybrid model for long-duration welding

The computationally efficient hybrid approach was developed to simulate a long duration UMW process and its subsequent cooling cycle. DEFORM-3D is a practical and efficient software package specially designed to simulate the 3D flow of complex metal forming processes. It uses a powerful adaptive remeshing technique during the simulation process [47,48], which effectively addressed the high-fidelity model limitation in excessive element distortions subject to severe plastic deformation. However, its implicit time integration method suffered from a prohibitively high computation cost when 20 kHz vibration loading was directly applied as model input. The hybrid model in this work combined the strengths of both ABAQUS and DEFORM-3D packages and ensured the simulation of the long duration UMW process while maintaining the simulation accuracy by using the high-fidelity ABAQUS model results as its inputs.

A two-step procedure was implemented in the hybrid model. The first step involved the high-fidelity ABAQUS/Explicit simulation for the initial short period, e.g., 0.2 s, of the UMW process. In the second step, the DEFORM-3D model simulates the whole UMW process from the beginning with model inputs calibrated from the high-fidelity model. The high-fidelity model outputs from Step 1 helped calibrate the inputs to the DEFORM-3D model in Step 2, which are described as follows:

(1) Equivalent z-displacement history of horn calibrated from the high-fidelity simulation;
(2) Equivalent heat flux calibrated from the high-fidelity simulation;
(3) A reduced frequency (e.g., 50 Hz) in-plane horn vibration.

These equivalent loadings were determined from the high-fidelity ABAQUS model simulation for a 0.2 s weld duration. The equivalent horn z-displacement loading was determined by extrapolating the high-fidelity simulation result to the whole weld duration. The heat generation for the frictional heat dissipation due to the 20-kHz horn vibration was determined from the friction heat dissipation for the whole model over a welding duration of 0.2 s simulated using ABAQUS/Explicit. The frictional heat dissipation rate was determined following the thermal analysis. Then, the ABAQUS/Explicit simulated heat dissipation rate was applied to the contact area between the horn and topmost tab in the DEFORM-3D model. The effects of a 20-kHz horn vibration loading therefore were well considered using the equivalent horn Z-displacement history, equivalent heat generations, and acoustic softening on the flow stress of coupon materials. Although a 20-kHz horn vibration input made the DEFORM-3D simulation non-convergent, a reduced frequency horn vibration, e.g., 50 Hz, with the same vibration amplitude can be applied in the model to account for the horn vibrating movement. The reduced frequency horn vibration loading was directly defined as temporal displacement history in DEFORM by tabular data.

3.3. Material constitutive model under ultrasonic loading

The material flow stress during UMW was determined from three competing mechanics, including material hardening with increased straining due to high frequency cyclic loading, thermal softening due to heat generation at the interface, and acoustic softening caused by ultrasonic vibration. The fundamental constitutive equations for the cyclic plasticity model that includes isotropic hardening and kinematic hardening terms were adopted from uniaxial loading. The effect of thermal softening was incorporated in the calculation of isotropic hardening and kinematic hardening model by inserting the temperature term $\left[1-\left(\frac{T-Tr}{Tm-Tr}\right)^m\right]$ [49]. To incorporate the acoustic softening effect in the flow stress calculation, a phenomenological softening term $[(1-duEu)^e]$ was introduced. This acoustic softening term was a function of the ultrasonic energy density per unit time [40]. After the inclusion of the thermal softening and acoustic softening terms, the modified equations of isotropic and kinematic hardening are given by [50]:

$$R_{ultrsonic} = \left[Q\left(1-e^{-b\bar{\varepsilon}^{pl}}\right)\right]\left[1-\left(\frac{T-T_r}{T_m-T_r}\right)^m\right]\left[(1-d_uE_u)^e\right] \quad (1)$$

$$\underline{\alpha_{ultrsonic}} = \left[\frac{C}{\gamma}\left(1-e^{-\gamma\bar{\varepsilon}^{pl}}\right)+\alpha_1 e^{-\gamma\bar{\varepsilon}^{pl}}\right]\left[1-\left(\frac{T-T_r}{T_m-T_r}\right)^m\right]\left[(1-d_uE_u)^e\right] \quad (2)$$

where d_u and e are the material constants related to ultrasonic softening and E_u is the ultrasonic energy density per unit time transferred from the horn to the material. The material constant values of copper are given in Table 2. These values were calibrated from experimental work for cyclic loading on copper [51], except that *e* was adopted from the previous simulation work of ultrasonic seam welding [40]. E_u was adopted as 3 .

Table 2
Material parameters in the flow stress model [40,51].

Q (MPa)	b	C (MPa)	γ	m	T_m (°C)	T_r (°C)	d_u (m^2/W)	E_u (W/m^2)	e
40	11	22,300	340	1.09	1083	25	1.3e-6	3.5e5 for tabs 8.1e4 for busbar	2

5×10^5 W/m^2 for tab layers, while a smaller E_u of 8.1×10^4 W/m^2 was assumed for the busbar which was subjected to less acoustic softening. As a result, the flow stress of the tab material softened approximately 50 %, while that of the busbar material softened approximately 30 %.

4. Simulation results and discussions

4.1. Dynamic welding simulation by high-fidelity model

The dynamic welding force simulation was compared with experimental measurements, which were acquired at a high sampling frequency, refer to as shown in Fig. 1, using the Kistler® SlimLine load cell. Fig. 4a is a snapshot of the simulation of dynamic welding force for a short period (0.4 – 0.405 s) in the out of plane direction from the high-fidelity model. The force oscillated in a sinusoidal fashion about a mean value of 1500 N with an oscillation amplitude varying from 150 N to 300 N. The average vertical force magnitude predicted from the ABAQUS model agreed well with the measurement data. A Fourier analysis of the force simulation data also indicated that the high-fidelity model correctly captured the 20 kHz fundamental frequency imposed by the horn vibration. It is the first attempt to the authors' best knowledge to validate the UMW process model using the high-frequency welding force data.

A more detailed comparison (cycle by cycle) of simulated Z-force and experimentally measured force signal is presented in Fig. 4b. It can be clearly seen that the frequency of the simulated Z-force matches the measured force signal. However, the simulated force oscillation amplitudes were significantly lower than those experimentally observed. The experimental measurement system demonstrated a much lower stiffness and resulted in a higher oscillation amplitude, approximately 1000 N (varying between 500 N and 2500 N), refer to Fig. 1. Similarly, it was

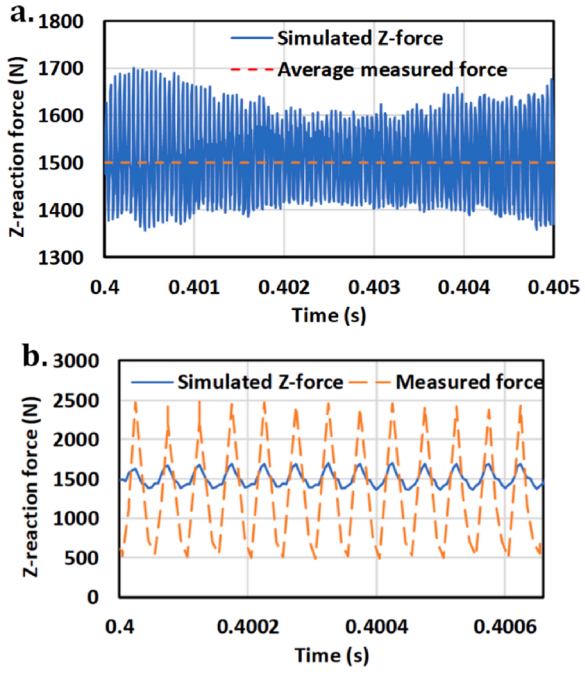

Fig. 4. High-fidelity model simulation under 8 μm amplitude horn vibration; (a) 20 kHz welding force in z-direction; (b) zoom in comparison of experimental and simulated force signal.

also experimentally observed during the vibration displacement measurement using the laser vibrometer that the amplitude of the out-of-plane horn vibration increased from just a few microns under the normal welding condition of a conventional welder system (without force sensors) to 0.6 mm under the experimental measurement system. The stiffness reduction in the welder in-situ measurement system was primarily due to the inclusion of the Kistler® SlimLine load cell between the anvil and mounting plate, refer to Fig. 1, which consequently resulted in a high-amplitude oscillation in both force and vibration data. However, for the current in-situ monitoring system, it was extremely challenging to acquire the high-frequency dynamic welding force history without significantly compromising the welder system stiffness. Based on the above analysis, the high-fidelity ABAQUS model developed in this study is considered adequate to predict the high-frequency dynamic force in the UMW process.

Fig. 5 presents screenshots of the simulation contours for von Mises stress and equivalent plastic strains in the work materials during the UMW process after 0.2 s of welding duration. The stress was highest at the peak and valley of the indentation here the plastic deformation was maximum (Fig. 5a). It was found that the plastic strain in the vibration direction was compressive on the side of the peak in which the knurl was moving whereas tensile on the opposite side (Fig. 5b). This indicates that the knurl pattern compressed the tab on one side and released the compression on other side of the peak within one oscillation cycle. The out-of-plane strain was tensile on the peaks of the deformed area as the material was subjected to flow in that direction. Conversely, it was compressive on the valleys as the material was pressed against the other tabs and busbar (Fig. 5c). Fig. 5d shows the comparison of deformation behavior of all the layers in terms of plastic strain in the out of plane direction after 0.2 s of the welding duration. As the top tab has direct contact with the vibrating horn, it endured the most severe plastic deformation with tensile and compressive plastic strain of 0.42 (at the peak) and 0.84 (at the valley), respectively at the deformed area (Fig. 5c). The severity of plastic deformation went down gradually in tab2 and tab3. There is no distinct peak and valleys of the deformed areas in those two layers and the plastic strain also went down one order compare with the top layer (Fig. 5d (T2 and T3)). However, the locations of the tensile and compressive plastic strain remain at the same areas under the top tab. The top side of the bus also has relatively low plastic deformation (Fig. 5d (B)).

The heat generation during UMW was evaluated with the high-fidelity model using three history outputs, namely, friction heat dissipation (FD), plastic deformation heat dissipation (PD), and internal heat energy (IHE). As it can be observed in Fig. 6a, the change of internal heat energy (ΔIHE) was equal to the sum of friction heat dissipation and plastic heat dissipation. The plastic heat dissipation accounts for 1 %–4 % of the friction heat dissipation, which means that the friction heat dissipation provided at least 95 % of the internal energy for the temperature rise in the whole system. Fig. 6b is a plot of rate of friction heat dissipation and plastic deformation heat dissipation versus time, which are time derivatives of the simulated heat dissipation. From the results it can be seen that the friction heat dissipation rate slightly decreased during the 0.2 s welding duration, while the plastic deformation heat dissipation rate increased during the process. But, the magnitude of friction heat dissipation rate was still significantly greater than that of the plastic deformation heat dissipation. In addition, it was found that the peak temperature was located at the interface between the horn and the tab in the ABAQUS/Explicit simulation, indicating that the friction between the horn and the tab contributed to the majority of the heat dissipation. In addition, in reference to Fig. 6c, the peak temperature

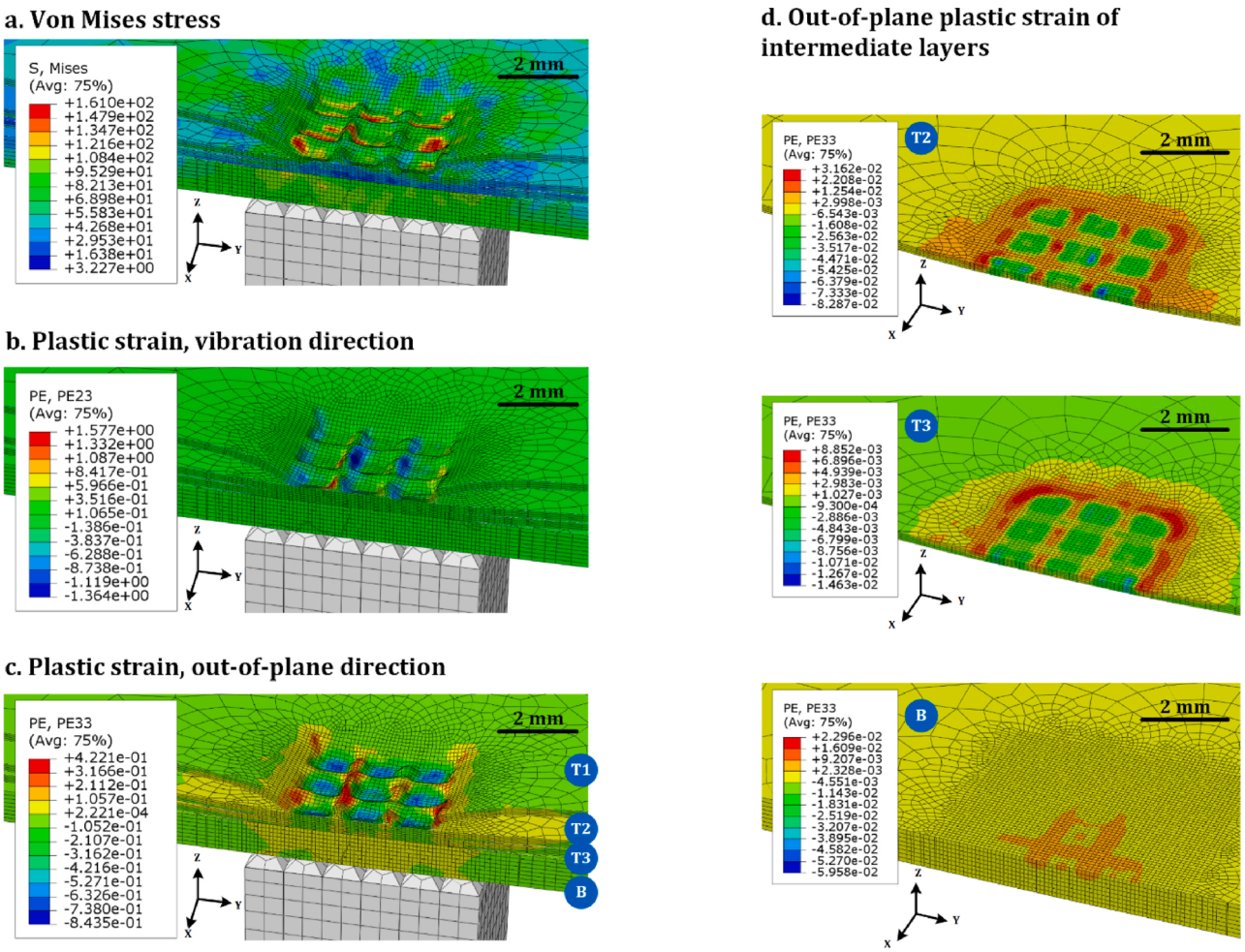

Fig. 5. 3D high-fidelity simulation of UMW process variables: (a) Von Mises stress in MPa; (b) plastic strain in vibration direction; (c) plastic strain in the out-of-plane direction; and (d) plastic strain in the out-of-plane direction of intermediate tab layers (T2 and T3) and busbar (B) [The scalebar represents dimension in Y direction].

was located at the interface between the horn and the tab in the ABAQUS/Explicit simulation, indicating that the friction between the horn and the tab contributed to the majority of the heat dissipation.

However, due to severe element distortions in the topmost tab layer, the simulation time of the high-fidelity model was limited to less than 0.45 s when the horn vibration amplitude was 8 μm. The model could only simulate up to 0.2 s when the horn vibration amplitude increased to 30 μm. Hence, the high-fidelity model is capable of simulating the long duration welding process. Nonetheless, this model can simulate the deformation and heat generation in the weld zone, dynamic welding force, horn displacement, metal slippage, material stress, strain, and strain rate. These predictions also provided critical loading inputs for DEFORM-3D simulation in the hybrid approach.

4.2. Long duration welding simulation by hybrid model

The hybrid model was able to simulate the long duration UMW process without directly modeling the 20 kHz dynamic attributes. Fig. 7 shows the dynamic welding force history over a 0.6 s welding period of the DEFORM-3D simulation. It correctly predicted an average welding force of 1500 N, while underestimating the oscillation in force compared with the high-fidelity ABAQUS model. It is worth noting that the sudden decrease in force for the DEFORM simulated force history at approximately 0.46 s was a result of a temporary contact area loss due to simulated material damage in the topmost tab. The force simulation restored to the nominal value when the tab deformed, and a full horn-tab contact was established again.

The temperature simulation of the long duration UMW process was validated using the temperature measurements as presented in Fig. 1. Fig. 8a is a plot of the DEFORM-3D simulated temperature histories over both welding duration and cooling cycle at different locations, i.e., P1– at the center of the tab/bus interface; P2 – close to the edge on the bus top surface; P3 – a position in the anvil. Fig. 8b is a plot of the experimentally measured temperature histories at P2 and P3, which were measured using IR camera and thermocouple, respectively. The comparison of the simulated and measured temperature histories exhibited a positive result on the temperature prediction, validating the method of equivalent heat generation for the hybrid approach.

4.3. Weld geometry simulation

The results of both the high-fidelity and hybrid model simulations identified that the top tab material between the knurl tips bulged and gradually filled the cavity of the knurl pattern due to the ultrasonic horn vibration, and the thickness gradually decreased for the material below the knurl tip. Meanwhile, the top tab material beyond the knurl pattern gradually deflected upward due to the combined effect of compression and ultrasonic horn vibration. Fig. 9 is a comparison of the simulated weld zone geometry to the micrograph of the corresponding experimental welds on the short-axis section (4.2 bar clamping pressure, 25 μm amplitude, and 2400 J ultrasonic energy). Comparing Fig. 9a and c, the simulated deformed geometry was very close to the micrograph in this section. Comparing Fig. 9b and d, it shows that this model can even capture the kink near the boundary of the weld zone. Fig. 9b also shows

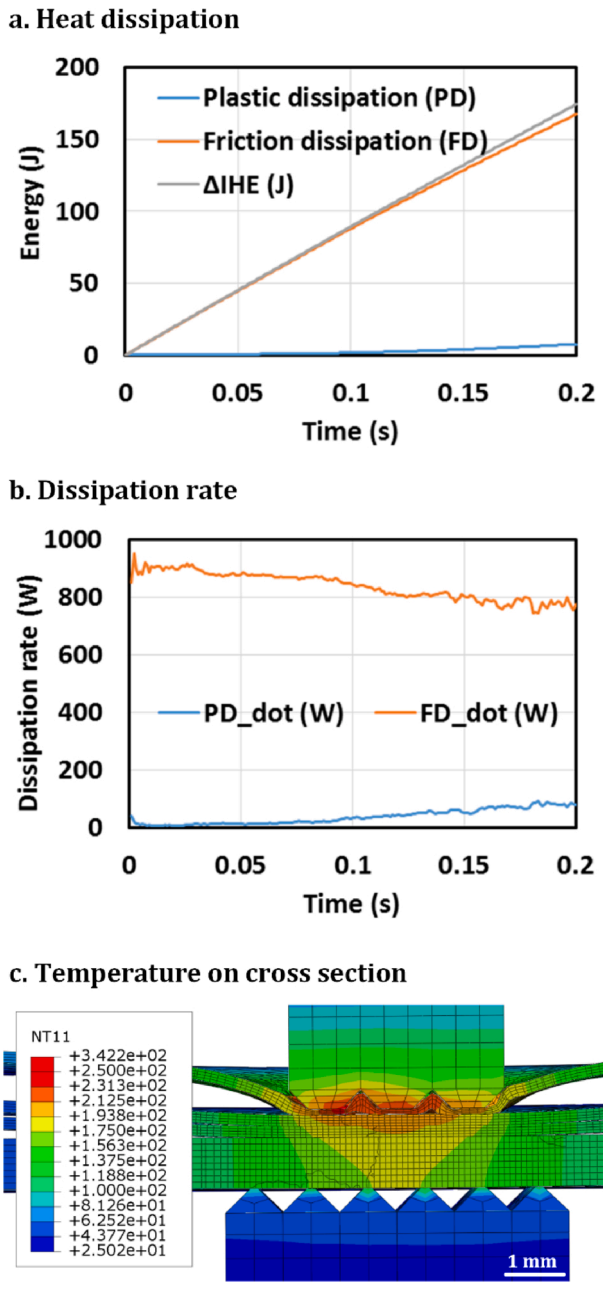

Fig. 6. Simulated heat generation: (a) histories of heat dissipation and internal heat energy change; (b) calculated heat dissipation rate histories; (c) temperature distribution on the cross section, which shows the heat dissipation mainly occurred at the topmost tab layer.

some small gaps between the topmost and second tab layers. This is attributed to the short simulation time of 0.2 s. These results support the conclusion that the deformation on the short-axis section was greater and occurred earlier due to the horn vibration, while it would take more time for the tab materials to coalesce on the long-axis section. This trend can be seen in another comparison to the laser-scan measured weld spot surface profile, refer to Fig. 10, which shows an excellent agreement between the simulation results and experimental data.

As it can be seen in the above discussions, the 3D models developed from this work can evaluate the effectiveness (e.g., deformation or heat generation) of a new knurl pattern for horn/anvil tools to narrow down the design choices without expensive tooling and prototyping. Likewise, the model can simulate the effect of any change in raw material or form factors. These simulation results can be very useful to significantly

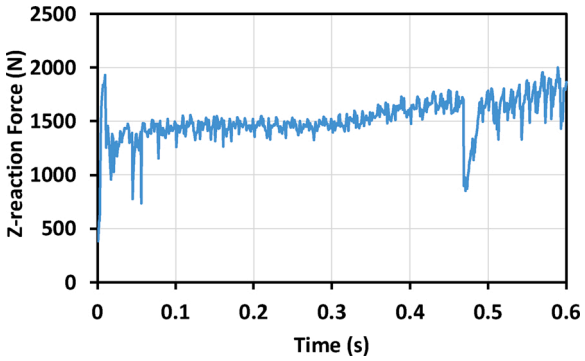

Fig. 7. Hybrid model (DEFORM-3D) simulation of dynamic welding force history using.

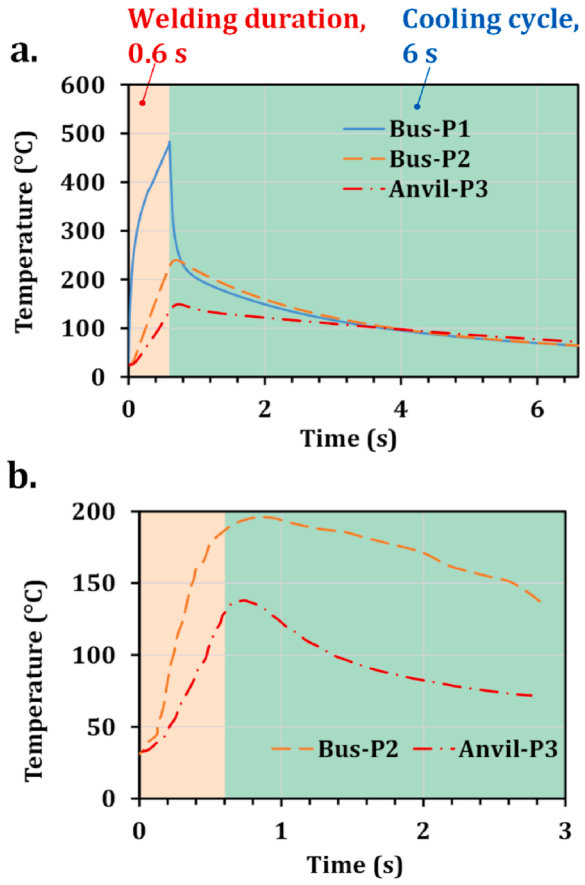

Fig. 8. Comparison of the DEFORM simulated temperature histories and the experimental measured at multiple locations: (a) DEFORM simulated and (b) experimental measured temperature histories.

shorten the learning curve for design engineering and understand the concerns from manufacturing engineering for the process development. This modeling work is more meaningful for a complicated process like UMW, which is very difficult to implement all necessary in-process transient monitoring with a high sampling frequency.

5. Conclusions

Two 3D finite element models were developed in this work to simulate the dynamic process of multilayer UMW process.

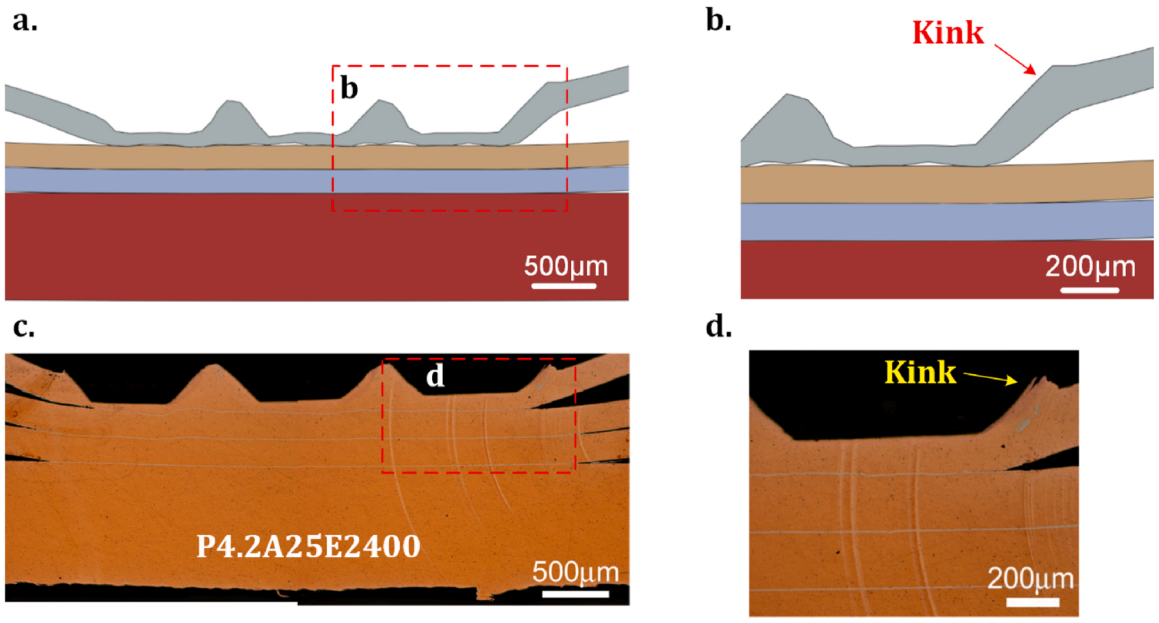

Fig. 9. High-fidelity ABAQUS model simulation of weld zone geometry compared with the micrographs on the short-axis section (horn vibration is within the section): (a) simulated weld zone geometry and (b) its zoom-in view at the right imprint; (c) optical micrograph of weld zone geometry and (d) its zoom-in view at the right imprint.

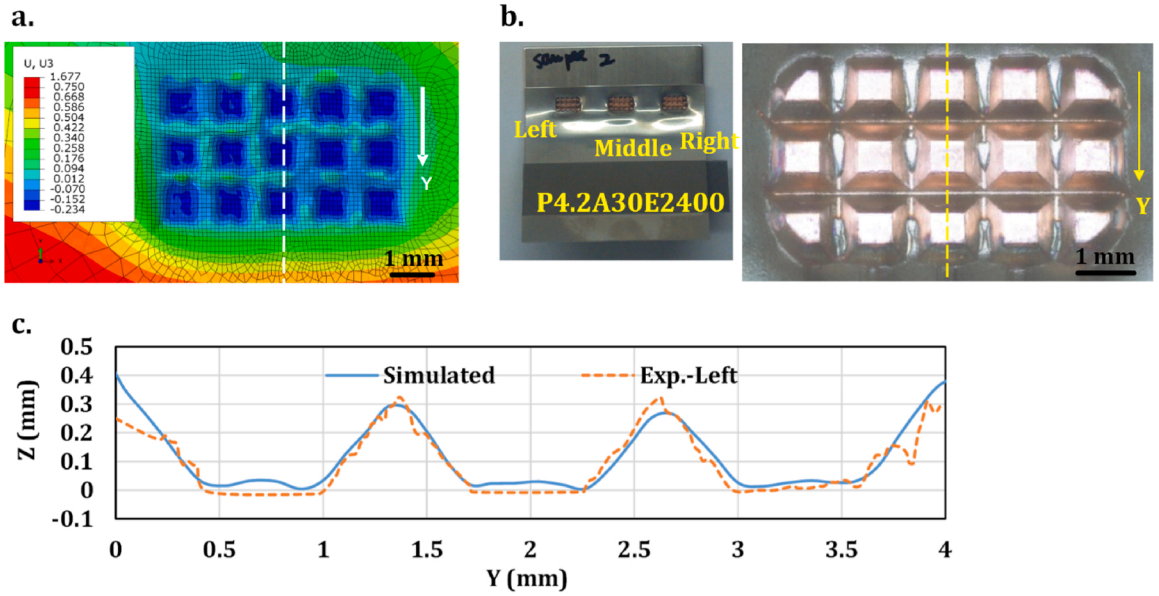

Fig. 10. Deformation results compared with the laser-scanned surface profile (1500 N clamping force and 30 μm amplitude): (a) the simulated out-of-plane direction deformation contour; (b) weld spot (original image adopted from [30]); (c) comparison of the simulated and laser-scan measured weld spot surface profile.

- For a short welding duration of 0.1−0.5 s, a high-fidelity FE modeling approach was developed using ABAQUS/Explicit to simulate dynamic material response under a 20 kHz horn vibration during UMW process. This portion of the simulation generates the most accurate FE results for the transient welding process since it models the actual cycle-by-cycle process dynamics.
- For an extended welding duration of more than 0.5 s, a computationally efficient hybrid approach was developed using both ABAQUS/Explicit and DEFORM to take advantage of the strengths of the two software packages. The DEFORM simulation used time-scaled welding cycles to reduce the computational cost associated with the expensive cycle-by-cycle simulations in ABAQUS/Explicit.
- Both models were validated using experimental measurements of UMW in terms of welding forces, temperatures and weld geometry.

The 3D numerical procedure developed in this study is the most comprehensive solution to date to simulate the complex material response during the UMW process and provides scientific understanding and engineering guidelines for improved the quality of ultrasonic weld battery packs. In the future work, the 3D model can be applied to facilitate the welding process development and reduce uncertainty by performing simulations with low and upper bounds of input process parameters. Empirical correlations could also be established between the weld quality and the simulations including dynamic material behaviors, temperature distribution, or thermal histories.

Declaration of Competing Interest

The authors declare that they have no known competing financial interests or personal relationships that could have appeared to influence the work reported in this paper.

Acknowledgments

The authors gratefully acknowledge the financial support by the National Science Foundation under NSF INTERN program under Grant Number CMMI-1537512.

References

[1] Cai W, Kang BS, Hu SJ. Ultrasonic welding of lithium-ion batteries. ASME Press; 2017. https://doi.org/10.1115/1.861257.
[2] Lee SS, Kim T-H, Hu SJ, Cai WW, Abell JA, Li J. Characterization of joint quality in ultrasonic welding of battery tabs. ASME J Manuf Sci Eng 2013;135:021004. https://doi.org/10.1115/1.4023364.
[3] Kicukov E, Gursel A. Ultrasonic welding of dissimilar materials: a review. Period Eng Nat Sci 2015;3:28–36. https://doi.org/10.21533/pen.v3i1.44.
[4] Takahashi Y, Inoue M. Numerical study of wire bonding - Analysis of interfacial deformation between wire and pad. J Electron Packag Trans ASME 2002;124:27–36. https://doi.org/10.1115/1.1413765.
[5] Long Y, He B, Cui W, Ji Y, Zhuang X, Twiefel J. Investigations on the mechanism of microweld changes during ultrasonic wire bonding by molecular dynamics simulation. Mater Des 2020;192:1–21. https://doi.org/10.1016/j.matdes.2020.108718.
[6] Li H, Cao B. Effects of welding pressure on high-power ultrasonic spot welding of Cu/Al dissimilar metals. J Manuf Process 2019;46:194–203. https://doi.org/10.1016/j.jmapro.2019.07.018.
[7] Yang JW, Cao B, He XC, Luo HS. Microstructure evolution and mechanical properties of Cu–Al joints by ultrasonic welding. Sci Technol Weld Join 2014;19:500–4. https://doi.org/10.1179/1362171814Y.0000000218.
[8] Panteli A, Robson JD, Brough I, Prangnell PB. The effect of high strain rate deformation on intermetallic reaction during ultrasonic welding aluminium to magnesium. Mater Sci Eng A 2012;556:31–42. https://doi.org/10.1016/j.msea.2012.06.055.
[9] Kang B, Cai W, Tan C-A. Vibrational energy loss analysis in battery tab ultrasonic welding. SME J Manuf Process 2014;16:218–32. https://doi.org/10.1016/j.jmapro.2013.10.008.
[10] Kang B, Cai W, Tan C-A. Dynamic stress analysis of battery tabs under ultrasonic welding. ASME J Manuf Sci Eng 2014;136:041011. https://doi.org/10.1115/1.4026990.
[11] Lee SS, Shao C, Kim T-H, Hu SJ, Kannatey-Asibu E, Cai WW, et al. Characterization of ultrasonic metal welding by correlating online sensor signals with weld attributes. ASME J Manuf Sci Eng 2014;136:051019. https://doi.org/10.1115/1.4028059.
[12] Zhao N, Li W, Cai WW, Abell JA. A fatigue life study of ultrasonically welded lithium-ion battery tab joints based on electrical resistance. ASME J Manuf Sci Eng 2014;136:051003. https://doi.org/10.1115/1.4027878.
[13] Xu L, Wang L, Chen Y-C, Robson JD, Prangnell PB. Effect of interfacial reaction on the mechanical performance of steel to aluminum dissimilar ultrasonic spot welds. Metall Mater Trans A 2016;47:334–46. https://doi.org/10.1007/s11661-015-3179-7.
[14] Zhao YY, Li D, Zhang YS. Effect of welding energy on interface zone of Al–Cu ultrasonic welded joint. Sci Technol Weld Join 2013;18:354–60. https://doi.org/10.1179/1362171813Y.0000000114.
[15] Dhara S, Das A. Impact of ultrasonic welding on multi-layered Al–Cu joint for electric vehicle battery applications: a layer-wise microstructural analysis. Mater Sci Eng A 2020;791:139795. https://doi.org/10.1016/j.msea.2020.139795.
[16] Das A, Masters I, Williams D. Process robustness and strength analysis of multi-layered dissimilar joints using ultrasonic metal welding. Int J Adv Manuf Technol 2019;101:881–900. https://doi.org/10.1007/s00170-018-2936-3.
[17] Zhang Z, Wang K, Li J, Yu Q, Cai W. Investigation of interfacial layer for ultrasonic spot welded aluminum to copper joints. Sci Rep 2017;7:12505. https://doi.org/10.1038/s41598-017-12164-2.
[18] Beyer W. The bonding process in the ultrasonic welding of metals. Schweisstechnik 1969;19:16–20.
[19] Watanabe T, Sakuyama H, Yanagisawa A. Ultrasonic welding between mild steel sheet and Al–Mg alloy sheet. J Mater Process Technol 2009;209:5475–80. https://doi.org/10.1016/j.jmatprotec.2009.05.006.
[20] Watanabe A, Yanagisawa T, Konuma S, Yoneda A, Ohashi O. Effect of oxide film on the strength of an ultrasonically welded joint and welding process - study of the ultrasonic welding of dissimilar metals (2nd report). Weld Int 1999;13:936–44. https://doi.org/10.1080/09507119909452077.
[21] Samanta A, Xiao S, Shen N, Li J, Ding H. Atomistic simulation of diffusion bonding of dissimilar materials undergoing ultrasonic welding. Int J Adv Manuf Technol 2019. https://doi.org/10.1007/s00170-019-03582-9.
[22] Guo W, Shao C, Kim TH, Hu SJ, Jin J, Spicer JP, et al. Online process monitoring with near-zero misdetection for ultrasonic welding of lithium-ion batteries: An integration of univariate and multivariate methods. J Manuf Syst 2016;38:141–50. https://doi.org/10.1016/j.jmsy.2016.01.001.
[23] Lee SS, Kim T-H, Hu SJ, Cai WW, Abell JA. Analysis of weld formation in multilayer ultrasonic metal welding using high-speed images. ASME J Manuf Sci Eng 2015;137:031016. https://doi.org/10.1115/1.4029787.
[24] Zhao J, Li H, Choi H, Cai W, Abell JA, Li X. Insertable thin film thermocouples for in situ transient temperature monitoring in ultrasonic metal welding of battery tabs. SME J Manuf Process 2013;15:136–40. https://doi.org/10.1016/j.jmapro.2012.10.002.
[25] Lu Y, Song H, Taber GA, Foster DR, Daehn GS, Zhang W. In-situ measurement of relative motion during ultrasonic spot welding of aluminum alloy using Photonic Doppler Velocimetry. J Mater Process Technol 2016;231:431–40. https://doi.org/10.1016/j.jmatprotec.2016.01.006.
[26] Ma Z, Zhang Y. Characterization of multilayer ultrasonic welding based on the online monitoring of sonotrode displacement. J Manuf Process 2020;54:138–47. https://doi.org/10.1016/j.jmapro.2020.03.007.
[27] Shao C, Hyung Kim T, Jack Hu S, (Judy) Jin J, Abell JA, et al. Tool wear monitoring for ultrasonic metal welding of lithium-ion batteries. J Manuf Sci Eng 2015;138:051005. https://doi.org/10.1115/1.4031677.
[28] Zerehsaz Y, Shao C, Jin J. Tool wear monitoring in ultrasonic welding using high-order decomposition. J Intell Manuf 2019;30:657–69. https://doi.org/10.1007/s10845-016-1272-4.
[29] Du P, Chen W, Deng J, Li K, Liu Y. Effects of knurl tooth angle on mechanical and thermal behaviors of aluminum ultrasonic welding. Ultrasonics 2020:106207. https://doi.org/10.1016/j.ultras.2020.106207.
[30] Lee D, Cai W. The effect of horn knurl geometry on battery tab ultrasonic welding quality: 2D finite element simulations. J Manuf Process 2017;28:428–41. https://doi.org/10.1016/j.jmapro.2017.04.009.
[31] Huang H, Chen J, Lim YC, Hu X, Cheng J, Feng Z, et al. Heat generation and deformation in ultrasonic welding of magnesium alloy AZ31. J Mater Process Technol 2019;272:125–36. https://doi.org/10.1016/j.jmatprotec.2019.05.016.
[32] Jedrasiak P, Shercliff HR. Finite element analysis of heat generation in dissimilar alloy ultrasonic welding. Mater Des 2018;158:184–97. https://doi.org/10.1016/j.matdes.2018.07.041.
[33] Elangovan S, Semeer S, Prakasan K. Temperature and stress distribution in ultrasonic metal welding—an FEA-based study. J Mater Process Technol 2009;209:1143–50. https://doi.org/10.1016/j.jmatprotec.2008.03.032.
[34] Langenecker B. Effects of ultrasound on deformation characteristics of metals. IEEE Trans Sonics Ultrason 1966;13:1–8. https://doi.org/10.1109/T-SU.1966.29367.
[35] Langenecker B. Work-softening of metal crystals by alternating the rate of glide strain. Acta Metall 1961;9:937–40. https://doi.org/10.1016/0001-6160(61)90112-2.
[36] Siu KW, Ngan AHW, Jones IP. New insight on acoustoplasticity – Ultrasonic irradiation enhances subgrain formation during deformation. Int J Plast 2011;27:788–800. https://doi.org/10.1016/j.ijplas.2010.09.007.
[37] Siu KKW, Ngan AHWA. Understanding acoustoplasticity through dislocation dynamics simulations. Philos Mag 2011;91:4367–87. https://doi.org/10.1080/14786435.2011.606237.
[38] Siu KW, Ngan AHW. Oscillation-induced softening in copper and molybdenum from nano- to micro-length scales. Mater Sci Eng A 2013;572:56–64. https://doi.org/10.1016/j.msea.2013.02.037.
[39] Malaki M, Ding H. A review of ultrasonic peening treatment. Mater Des 2015;87:1072–86. https://doi.org/10.1016/j.matdes.2015.08.102.
[40] Siddiq A, Ghassemieh E. Thermomechanical analyses of ultrasonic welding process using thermal and acoustic softening effects. Mech Mater 2008;40:982–1000. https://doi.org/10.1016/j.mechmat.2008.06.004.
[41] Siddiq A, Ghassemieh E. Theoretical and FE analysis of ultrasonic welding of aluminum alloy 3003. ASME J Manuf Sci Eng 2009;131:041007. https://doi.org/10.1115/1.3160583.
[42] Lee D, Kannatey-Asibu E, Cai W. Ultrasonic welding simulations for multiple layers of lithium-ion battery tabs. ASME J Manuf Sci Eng 2013;135:061011. https://doi.org/10.1115/1.4025668.
[43] Shen N, Samanta A, Ding H, Cai WW. Simulating microstructure evolution of battery tabs during ultrasonic welding. SME J Manuf Process 2016;23:306–14. https://doi.org/10.1016/j.jmapro.2016.04.005.
[44] Li H, Cao B, Liu J, Yang J. Modeling of high-power ultrasonic welding of Cu/Al joint. Int J Adv Manuf Technol 2018;97:833–44. https://doi.org/10.1007/s00170-018-2002-1.
[45] Chen K, Zhang Y, Wang H. Effect of acoustic softening on the thermal-mechanical process of ultrasonic welding. Ultrasonics 2017;75:9–21. https://doi.org/10.1016/j.ultras.2016.11.004.
[46] Cai W, Blau PJ, Qu J. Friction coefficients of battery metals and the usage in ultrasonic welding simulations. World Electr Veh Symp Exhib (EVS27) 2013. https://doi.org/10.1109/EVS.2013.6914778. 2013:1–10.
[47] Li G, Yang J, Oh JY, Foster M, Wu W, Tsai P, et al. Advancements of extrusion simulation in DEFORM-3D. Proc. Int. Conf. Extrus. Benchmark 2009.
[48] Zhang D, Yang H, Sun Z, Fan X. A new FE modeling method for isothermal local loading process of large-scale complex titanium alloy components based on DEFORM-3D. AIP Conf Proc 2010;1252:439–46. https://doi.org/10.1063/1.3457588.

[49] Johnson G, Cook W. A constitutive model and data for metals subjected to large strains, high strain rates and high temperatures. Proc 7th Int Symp Ballist 1983: 541.

[50] Siddiq A, Sayed El T. A thermomechanical crystal plasticity constitutive model for ultrasonic consolidation. Comput Mater Sci 2012;51:241–51. https://doi.org/10.1016/j.commatsci.2011.07.023.

[51] Bower AF. Cyclic hardening properties of hard-drawn copper and rail steel. J Mech Phys Solids 1989;37:455–70. https://doi.org/10.1016/0022-5096(89)90024-0.